



Substantiating microCT for diagnosing bioerosion in archaeological bone using a new Virtual Histological Index (VHI)

Kirsten Mandl^{1,2} · Kellie Sara Duffett Carlson^{1,3} · David Brönnimann⁴ · Ashley McCall⁵ · Martin Grassberger^{1,6} · Maria Teschler-Nicola^{1,7} · Estella Weiss-Krejci^{2,8} · Brian Metscher⁹

Received: 13 January 2022 / Accepted: 17 April 2022
© The Author(s) 2022

Abstract

Recent technological advances have broadened the application of palaeoradiology for non-destructive investigation of ancient remains. X-ray microtomography (microCT) in particular is increasingly used as an alternative to histological bone sections for interpreting pathological alterations, trauma, microstructure, and, more recently, bioerosion with direct or ancillary use of histological indices. However, no systematic attempt has been made to confirm the reliability of microCT for histotaphonomic analysis of archaeological bone. The objective of this study is therefore to compare thin sections of human femora rated with the Oxford Histological Index to microCT sections using the newly developed Virtual Histological Index in order to provide an accessible methodology for the evaluation of bioerosion in archaeological bone. We provide detailed descriptions of virtual sections and assess the efficacy of the method on cranial and postcranial elements, cremated long bones, and faunal samples. The traditional histological and virtual methods showed a strong correlation, providing the first systematic data substantiating lab-based microCT as a suitable alternative tool for reconstructing post-mortem history in the archaeological record, and for the reliable, non-destructive screening of samples for further analyses.

Keywords Bone histology · MicroCT · Mortuary archaeology · Bioanthropology · Bioerosion · Histotaphonomy

Kirsten Mandl and Kellie Sara Duffett Carlson contributed equally to the research.

✉ Kellie Sara Duffett Carlson
kelliesard86@univie.ac.at

Kirsten Mandl
kirsten.mandl@univie.ac.at

David Brönnimann
david.broennimann@unibas.ch

Martin Grassberger
martin.grassberger@med.sfu.ac.at

Maria Teschler-Nicola
maria.teschler@nhm-wien.ac.at

Estella Weiss-Krejci
estella.weiss-krejci@oeaw.ac.at

Brian Metscher
brian.metscher@univie.ac.at

³ Human Evolution and Archaeological Sciences, University of Vienna, Vienna, Austria

⁴ Integrative Prehistory and Archaeological Science, Department of Environmental Sciences, University of Basel, Spalenring 145, 4055 Basel, Switzerland

⁵ Dublin, Ireland

⁶ Faculty of Medicine, Sigmund Freud University, Vienna, Austria

⁷ Department of Anthropology, Natural History Museum Vienna, Burgring 7, 1010 Vienna, Austria

⁸ Department of Social and Cultural Anthropology, University of Vienna, Universitätsstraße 7 (NIG), 1010 Vienna, Austria

⁹ Department of Evolutionary Biology Unit for Theoretical Biology, University of Vienna, Djerassiplatz 1, 1030 Vienna, Austria

¹ Department of Evolutionary Anthropology, University of Vienna, Djerassiplatz 1, 1030 Vienna, Austria

² Historical Archaeology, Austrian Archaeological Institute, Austrian Academy of Sciences, Franz-Klein-Gasse 1, 1190 Vienna, Austria

Introduction

As human remains offer unique perspectives on mortuary behaviour in the past, the continued development and testing of bioarchaeological methods and techniques play an important role in refining our understanding of long-term taphonomic processes. In recent years, numerous histotaphonomic studies of archaeological human and faunal bone have looked at bioerosion to understand the mechanisms by which a corpse turns into a skeleton (e.g. Smith et al. 2002; Turner-Walker and Peacock 2008; Fernández-Jalvo et al. 2010; Hollund et al. 2012, 2018; Booth 2016, 2017; Brönnimann et al. 2018). Although there is disagreement concerning the origin of bioeroding microorganisms and what histotaphonomic analysis can truly tell us about early taphonomic events (Parker Pearson et al. 2005; Kontopoulos et al. 2016; Turner-Walker 2019), such analyses have proven to be highly effective for assessing the presence and type of bioerosion in archaeological bone. To improve the accessibility of histotaphonomic research in archaeology, this paper tests the utility of lab-based microCT imaging and presents the Virtual Histological Index (VHI), which together provide a rapid and minimally destructive method for the reconstruction of the early post-mortem history of archaeological bone.

The restructuring of bone microanatomy by microorganisms such as fungi and bacteria is referred to as biogenic bone degradation, or bioerosion (Piepenbrink 1986; Turner-Walker 2012). Upon death, at the outset of the post-mortem interval, bone is beset by osteolytic microorganismal activity induced by the host's enteric microbiome and/or by microbiota in the burial environment, which affect its surface and microstructure, eroding the histological anatomy (Child 1995; Janaway 1996; Jans 2008; White and Booth 2014; Kontopoulos et al. 2016; Metcalf et al. 2016; Damann and Jans 2017; Brönnimann et al. 2018). This not only influences chemical and radiological analyses but is also—along with other factors such as the pH value of the soil—responsible for the fragile nature of archaeological skeletons (Millard 2001; Nielsen-Marsh et al. 2007). Differences in environmental and soil conditions may affect the proliferation of osteolytic bacteria or saprophagous organisms (Wedl 1865; Kendall et al. 2018).

Bioerosion can be separated into three broad categories (Wedl 1865; Hackett 1981; Jackes et al. 2001; Turner-Walker 2012) partly defined according to infill and size: (1) Wedl tunnelling type 1 (10–15 μm in diameter), (2) Wedl tunnelling type 2 (5 μm in diameter), and (3) osteolytic bacteria-induced non-Wedl tunnelling (Jans 2008; Brönnimann et al. 2018; Turner-Walker 2019). Osteolytic bacteria cause microscopic focal destructions (MFDs) that result from solubilization, leaching, or redistribution of

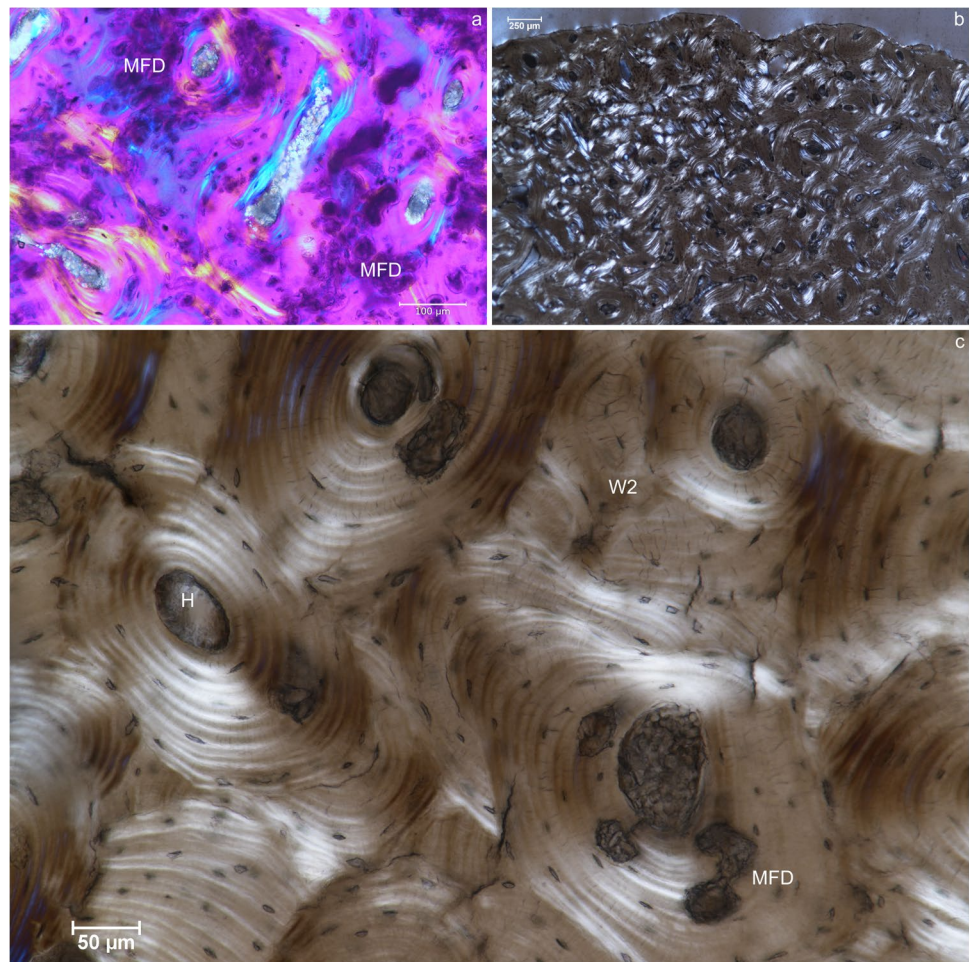
hydroxyapatite (HAp) (Fig. 1a, c) (Hackett 1981; Child 1995; Balzer et al. 1997; Jans 2008). Hackett (1981) further describes three categories of non-Wedl tunnelling that can be histologically differentiated by size, shape, lamellate content, and the presence or lack of a hypermineralized cuff: (a) linear longitudinal (5–10 μm in diameter); (b) budded (30–60 μm in diameter); and (c) lamellate (10–60 μm in diameter) (Jans et al. 2004; Jans 2008). However, the causal organism may be identical with differences resulting from local bone microarchitecture (Hackett, 1981). Specific organisms cannot easily be identified as causative agents based on the size or morphology of MFDs (Jans et al. 2004; Turner-Walker 2012; Kendall et al. 2018). However, osteolytic bacteria are the primary cause of bioerosion in archaeological human bone (Yoshino et al. 1991; Balzer et al. 1997; Jackes et al. 2001; Jans et al. 2004), with linear longitudinal and budded MFDs most frequently encountered, representing 85% of bacterial attack; lamellate tunnelling, which is less common, is infrequently found alone (Jans et al. 2004), and is observed surrounding the rim of the Haversian systems. Fungal tunnelling is less frequently observed in human than in animal bone, which may result from the influence of cooking, bone microarchitecture or porosity, or other taphonomic factors.

Background

Studies in the fields of palaeontology (Higgs et al. 2011) and anthropology (Le Garff et al. 2017) applied microCT to bone to identify different types of diagenesis, and in combination with histological indices (Dal Sasso et al. 2014; Booth et al. 2016), while others have used scanning electron microscopy (SEM) (Turner-Walker and Syversen 2002) or synchrotron radiation microCT (SR-microCT) (Caruso et al. 2020, 2021). Dal Sasso et al. (2014) and Booth et al. (2016) were amongst the first to see the value of lab-based microCT scanning for the evaluation of diagenetic alteration to archaeological bone, stating that virtual cross-sections are comparable to thin section micrographs as rated via the Oxford Histological Index (OHI). However, there has been no systematic attempt to confirm this, nor the broader utility of this technology for investigating microscopic diagenetic alterations in comparison to the well-established method of histotaphonomy.

MicroCT with commercial lab-based systems can produce detailed volume images of intact objects with microscopic resolutions. This obviously requires samples small enough to fit into the tomography setup, and in most commercial systems, the largest sample that can be imaged with ca. 5 μm voxels is 5 to 10 mm in diameter and 100 to 200 mm in length. Thus, the lab-based imaging we describe applies to small bones, bone fragments, or bone samples previously

Fig. 1 Light micrographs showing the described histological features. **a** Inhibited bioerosion (MFD) and exogenous mineral precipitation in canals in femoral sample S01. The blue and yellow visualize collagen birefringence. The micrograph was taken with a lambda plate and 10(2×) magnification. **b** Very good collagen preservation in femoral sample GÖ01. The micrograph was taken with cross polarised light and 10(1.5×) magnification. **c** Inhibited bioerosion around Haversian canals (H) with Wedl type 2 tunnelling (W2) identified by enlarged canaliculi in femoral sample GÖ01. The micrograph was taken with polarised light and 10(2×) magnification



prepared for sectioning. For objects with sufficient inherent X-ray contrast, such as bone, no preparation is required apart from stable mounting of the specimen.

Importantly, studies comparing microCT images with histology to evaluate skeletal trauma (Baier et al. 2019), pathological alterations (Rühli et al. 2007), bone morphometry (Uchiyama et al. 1997; Müller et al. 1998), and cortical bone microstructure (Particelli et al. 2012), identify strong correlations between conventional histological section methods and virtual assessments. Therefore, comparing bioerosion in thin sections with virtual sections is a crucial first step towards confirming the reliability of microCT for identifying microscopic taphonomic alterations to bone. The aim of this research is thus to systematically compare transverse thin sections rated with the OHI to microCT scan images rated with the newly developed VHI. In doing so, we contribute an accessible, minimally destructive investigative tool for reconstructing post-mortem history in the archaeological record, and for the reliable screening of samples for further analysis. Importantly, the method also permits assessment of the entire virtual sample, including individual virtual slices through the 3D image,

chosen locations within the sample, or larger virtual sections composed of several virtual slices in any orientation.

Materials and methods

Dataset and sampling

The dataset is based on 28 samples selected from five archaeological sites in the temperate European environment of Lower Austria dating from the Early Neolithic to Late Iron Age (Table 1). Studies have demonstrated intra-skeletal variation for diagenetic alteration, and that the cortex of long bones tends to best describe bioerosion (e.g. Jans et al. 2004; Dal Sasso et al. 2014; Booth 2017), which is likely due to the longitudinal alignment of osteons and collagen axes, which simplify the histology and direction of tunnelling. To facilitate comparison with previous research (e.g. Jans et al. 2004; White and Booth 2014; Booth 2017), samples 1–2 cm thick were preferentially extracted from the anterior aspect of the proximal femoral diaphysis ($n = 15$) inferior to the surgical neck. Rib

Table 1 Provenance and number of 28 cortical bone samples by period: femora ($n=15+5$ cremated), ribs ($n=2$), parietal ($n=2$), humerus ($n=1$), mandible ($n=1$), faunal long bones ($n=2$). For further details, see Supplementary Materials S1

Site	Sample date range	Archaeological culture	Period	No. of samples/individuals
Asparn-Schletz	5300–5000 BCE	Linear Pottery (LBK)	Early Neolithic	7/7
Gemeinlebarn A	2050–1650 BCE	Unterwöbling	Early Bronze Age	6/6
Inzersdorf ob der Traisen	1200–900 BCE	Urnfield (Ha A ₁ –Ha B ₁)	Late Bronze Age	4/4
Göttlesbrunn-Arbesthal	380–200 BCE	Early/Middle La Tène (LT B ₁ –LT B ₂ /C ₁)	Late Iron Age	7/5
Roseldorf-Sandberg	390–150 BCE	Early/Middle La Tène (LT B ₁ –LT C)	Late Iron Age	4/4

($n=2$), mandible ($n=1$), skull ($n=2$), and humerus ($n=1$) fragments were also selected to evaluate the efficacy of the method on non-femoral samples (Supplementary Materials S1). Five cremated long bones and two faunal mammalian long bones were also sampled. Samples were extracted with a diamond wheel blade attached to a Dremel® 3000 electric drill. The histological investigation was conducted using the well-established OHI (Hedges et al. 1995; Millard 2001), while the virtual assessment was completed using the newly developed VHI.

Statistics

Hedges et al. (1995) note the subjectivity inherent in rating samples with the OHI but found general agreement between observers within a single rating unit. This approach is applied here where we performed inter-rater reliability (IRR) tests between the two OHIs, between the two VHIs, and between the averaged OHIs and the averaged VHIs using the Pearson correlation coefficient (PCC), joint-probability of agreement (JPA), and limits of agreement (LOA). Overall IRR analysis, also known as inter-rater agreement or inter-observer reliability, is the degree to which there is agreement amongst independent observers rating the same phenomenon. The PCC is the linear correlation between two sets of data where it measures covariances, resulting in values ranging between -1 (highly uncorrelated) and $+1$ (highly correlated). JPA is the percentage of times that raters agree, and is the least robust measurement of IRR as it does not account for agreement based on chance. To compensate for this weakness, LOA was applied. This approach calculates the difference between each pair of observations with the mean value acting as the bias value ± 2 standard deviation (Bland and Altman 1986). This type of analysis provides insight into how much random variation influences the ratings, as depicted in the Bland–Altman plots. Furthermore, to assess the true scope of variation of agreement, the JPA calculations were evaluated for an exact match (identical observations), an approximate match (≤ 0.5 difference), and a

general match (≤ 1.0 difference). This approach captures the degree to which observers entirely agree (disregarding the principle of equifinality), and with applied thresholds for when observers somewhat and generally agree.

All statistical analyses were performed in R (v. 4.0.2). All figures were formatted using GIMP software (v. 2.99.6), and the SciFiFig plugin (Aigouy and Mirouse 2013) for Fiji software (Schindelin et al. 2012).

Light microscopy (LM) and scanning electron microscopy (SEM)

Twenty-four samples were selected for embedding in a two-compound resin (Biodur® E1/E2) following a protocol for undecalcified bone (Schultz 2001). The blocks were sectioned in the transverse plane with a Leica SP 1600 saw-blade microtome (Leica Microsystems) to a thickness ranging from 30 to 60 μm , and then mounted to a glass slide with Histokitt (ROTI®) and covered with a glass cover slip. A Nikon Eclipse Ni light microscope was used with $4\times$, $10\times$, and $20\times$ magnifications under plane light, polarised light (XPL), and differential phase contrast light. Additionally, a lambda plate was used with XPL to visualize collagen. Micrographs were taken with a DS-Ri2 camera (Nikon) mounted to the microscope. All visualizations were conducted with NIA Elements BR Software (Nikon). Six samples were mounted on carbon planchets and examined with an IT 300 LAB6 (JEOL Ltd.) scanning electron microscope at low vacuum at 25.0 kV under high magnification. Images were taken in backscatter electron mode.

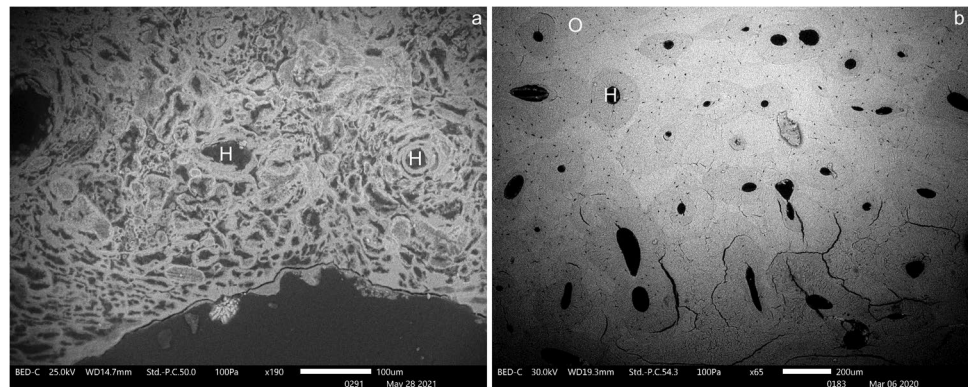
Oxford Histological Index (OHI)

The OHI (Table 2) was developed to determine the percentage of bone unaffected by bioerosion within a single cross-section using thick, polished sections as evaluated through reflected light microscopy by the application of an ordinal scale from zero, which indicates poor preservation without original features save for Haversian canals, to five, which indicates good preservation,

Table 2 Definitions of the Oxford Histological Index (OHI) (Hedges et al., 1995; Millard, 2001) and Virtual Histological Index (VHI)

OHI/VHI	% Intact bone	Description (thin sections)	Description (virtual sections)
5	> 95	Very well preserved, indistinguishable from fresh bone	Very well preserved, indistinguishable from fresh bone: canals and lamellae are clear; grey values are consistent within and between slices
4	> 85	Only minor amounts of destructive foci, otherwise generally well preserved	Only minor amounts of destructive foci, otherwise generally well preserved; small patches of MFD present (darker grey values). The canals and lamellae are easily distinguished throughout the stack
3	> 67	Clear preservation of some osteocyte lacunae	Destructive foci evident throughout stack but more than half of the bone remains unaffected; bioerosion spreads beyond lamellae in patches but the foci are still visible
2	< 33	Clear lamellate structures preserved between destructive foci	Destructive foci may still be present but bioerosion now primarily presents in wide swathes of dark grey values in which lamellae are nearly indistinguishable; in small unaffected or less affected regions, lamellae remain distinguishable; there is more affected bone than non-affected
1	< 15	Small areas of well-preserved bone, or some lamellar structures preserved by pattern of destructive foci	The majority of the stack is filled with bioerosion; only the smallest patches of MFD are distinguishable within a wide swathe of dark grey values; in most regions the lamellae have disappeared or are only vaguely distinguishable
0	< 5	No original features identifiable other than Haversian canals	Erosion is pervasive throughout and hardly any unaffected bone remains; lamellae are indistinguishable; only the slightest outline remains within the erosion; a small number of canals may still be present or may be completely obliterated

Fig. 2 SEM-BSE images of two femora. **a** Near complete destruction of microanatomy (OHI 0.5) by bioerosion with only Haversian canals (H) remaining in sample S02. **b** Perfectly preserved microanatomy (OHI 5) with clearly identifiable osteocyte lacunae (O) in sample GÖ04



like unaltered bone (Fig. 2) (Hedges et al. 1995; Millard 2001). Jans et al. (2002) made two modifications to the OHI to provide a more detailed examination by (1) using thin sections, and (2) dividing the sample transversely, according to anatomy, into periosteal, endosteal, and midline sections, and then assigning each an OHI (Jans 2008). In the present study, Jans et al.'s (2002)

modifications to the OHI were used to quantify bioerosion in samples via LM and SEM. Two observers separately assessed the thin sections using the OHI (Supplementary Materials S2).

X-ray microtomography (microCT)

The same samples from which thin sections were taken for LM and SEM were placed in plastic cylinders stabilized with synthetic foam prior to microCT scanning. Scans were made at the University of Vienna Theoretical Biology imaging lab using a Zeiss/Xradia MicroXCT-200 or a Bruker/SkyScan 1272 microCT system, with image resolutions ranging from 4 to 10.9 μm (isotropic voxel size), sufficient to image osteolytic bacteria-induced non-Wedl tunnelling. Further scanning specifications and parameters are outlined in Supplementary Materials S3.

Virtual Histological Index (VHI)

The VHI (Table 2) was designed to closely reflect the OHI; thus, the standard 0 to 5 ordinal scale was maintained. Evaluation of the originally stipulated anatomical and destructive features required some modification as absorption-contrast microCT cannot visualize, for example, individual concentric lamellae or osteocyte lacunae. Features that can be visualized, such as Haversian and Volkmann canals, undifferentiated lamellae, and MFD were retained. Given the relative similarity of what could be found in the virtual slices in comparison to traditional histology, no drastic modification of the OHI was required. Following Jans et al. (2002), we assigned individual OHIs to the periosteal, endosteal, and midline regions and then averaged the values to obtain a single VHI. Two observers separately assessed the scans using the VHI (Supplementary Materials S2).

Results

Eight of the twenty-eight samples were selected to report what can be visualized in virtual cross-sections in comparison to what was identified in the thin section micrographs as an introduction to how bioerosion presents at each level of the VHI. This subset consists of samples from the femur and mandible, and includes one faunal sample, a cremated sample, and a severely osteoporotic sample. Selected images

are included in the text while the remaining ones can be found in the Supplementary Materials (S4–S28).

SB01/mandibular ramus (OHI 5/VHI 5) (Fig. 3)

OHI with LM No MFD can be found in the entire thin section. There is reduced collagen content along the periosteal surface, but overall, collagen concentration is high. Enlarged lacunae and canaliculi, evidence of Wedl type 2 tunnelling, are visible throughout the entire thin section (Supplementary Material S4). The periosteal and endosteal surfaces are in good condition, and osteocyte lacunae are numerous. There is no damage to the microstructure. Sediment is visible along trabecular surfaces. A minority of the Haversian canals are filled with exogenous material.

Virtual cross-sections The bone is in nearly perfect condition with no visible bioerosion. Grey values remain consistent within and between slices through the volume image. Lamellae around Haversian canals are defined as the cement lines that surround them. There are inclusions within a small number of canals and attached to trabeculae, as noted in the histology, which are not to be confused with bioerosion.

GE15/femur (OHI 4/VHI 4.5) (Fig. 4)

OHI with LM The bacterial attack is arrested. The highest concentration of MFD is within the midline and endosteum; the trabeculae are affected and the periosteum mildly so. Microfissures follow the microanatomy along the periosteal surface. Collagen preservation is very good throughout the entire section. There is exogenous mineral precipitation within the Haversian systems, primarily along the endosteal surface with a milder manifestation along the midline.

Virtual cross-sections Bioerosion is minimal. Grey values are mostly consistent throughout and between virtual slices with minor density loss (darker grey values), particularly around the midline and towards the endosteal surface. Bioerosion is concentrated around Haversian systems with numerous MFDs present as small clusters of perforations

Fig. 3 Sample SB01, a late adult male. **a** Light micrograph of cortex and trabeculae in a transverse histological thin section (plane light under 4(1 \times) magnification). **b** Single virtual transverse cross-Sect. (1 voxel [8.0 μm] thick) through a microCT image showing midline, and endosteal surfaces

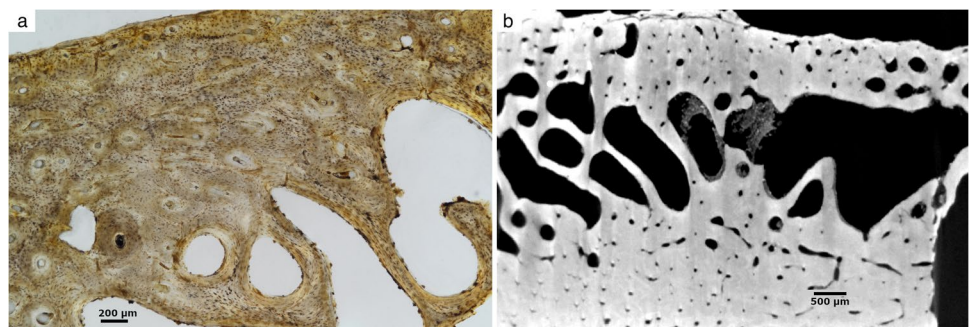
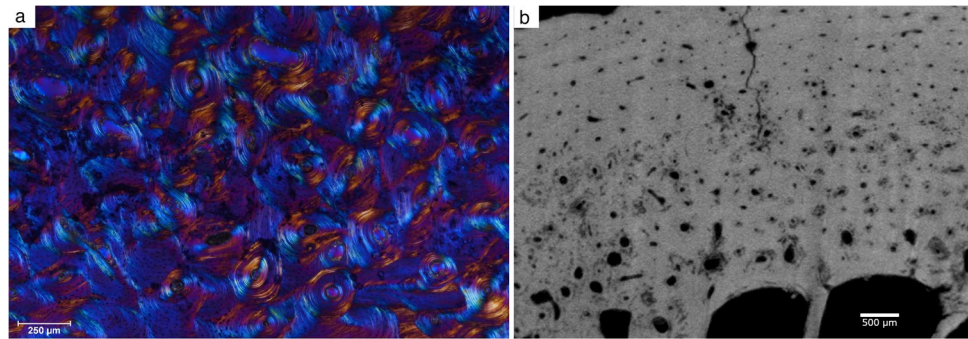


Fig. 4 Sample GE15, a mature male. **a** Light micrograph of midline of a transverse histological thin section (lambda plate under $4(1.5\times)$ magnification). **b** Single virtual transverse cross-Sect. (1 voxel [$8.0\ \mu\text{m}$] thick) through a microCT image showing midline, and periosteal and endosteal surfaces



forming speckled areas of demineralization. While individual lamellae are visually indistinct, undifferentiated concentric lamellae surrounding the Haversian canals remain visible. Some cement lines can be distinguished in the filter contrast-enhanced figure (Supplementary Material S5) as confirmed by assessment of multiple virtual slices. The periosteal circumferential lamellae are eroded more so than the endosteal lamellae, which have undergone microbial attack, as have the surfaces of the trabeculae. Microfissures that move from the periosteum towards the midline along the anatomy of the Haversian systems appear to be post-depositional or post-excavation damage as bioerosion does not follow them. There are inclusions in canals near the endosteum.

S01/femur (OHI 2.75/VHI 3) (Fig. 5)

OHI with LM Bioerosion is inhibited. MFD is equally dispersed throughout the entire section. Collagen preservation is mediocre though it is better within the unaffected lamellae. There are many enlarged canaliculi and lacunae, evidence of Wedl type 2 tunnelling. Most of the canals are filled with exogenous mineral precipitation. The endosteal surface is not eroded, though the periosteal surface is damaged.

Virtual cross-sections A moderate level of bioerosion is present. Canals can be distinguished throughout much of the bone; when not visible, it is not due to bioerosion; the sample is an early adult and much of the endosteal lamellae remain where at this age, fewer secondary osteons have

formed with cement lines. The periosteal lamellae are more heavily eroded. There are MFDs and patches of reduced density within the circumferential lamellae of the endosteal surface that connect with bioerosion surrounding Haversian systems. Lamellae of the Haversian canals are distinct within areas of relatively unaffected bone; the bioerosion, which presents as both MFD and patches of dark grey values, has primarily attacked the periosteum and the midline towards the periosteum. A large embedding artefact traverses the sample from the endosteum to the midline. Small patches of high density (white) material fill a few canals towards the endosteal surface and along the midline; the most external lamellae of the endosteum are also a higher density.

R03/femur (OHI 1/VHI 1.75) (Fig. 6)

OHI with LM Bioerosion is present throughout the entire section. MFD is strongest along the midline towards the endosteum. A large area along the midline towards the endosteum remains mostly unaltered with unaffected lamellae still visible, though there are MFDs around the Haversian canals. Within this area, collagen content is very good and the lacunae remain a normal size. All canals and microfissures are filled with calcite. A large microfissure runs from the periosteum of the entire section through the histological anatomy, which may be the result of shrinkage as the bone dries in areas where there is no tunnelling. Microfissures following the microanatomy travel from the periosteum into the midline. Sediment is attached to the periosteal surface.

Fig. 5 Sample S01, an early adult female. **a** Light micrograph of midline and endosteum of a transverse histological thin section (plane light under $4(1\times)$ magnification). **b** Single virtual transverse cross-Sect. (1 voxel [$8.0\ \mu\text{m}$] thick) through a microCT image showing midline, and periosteal and endosteal surfaces

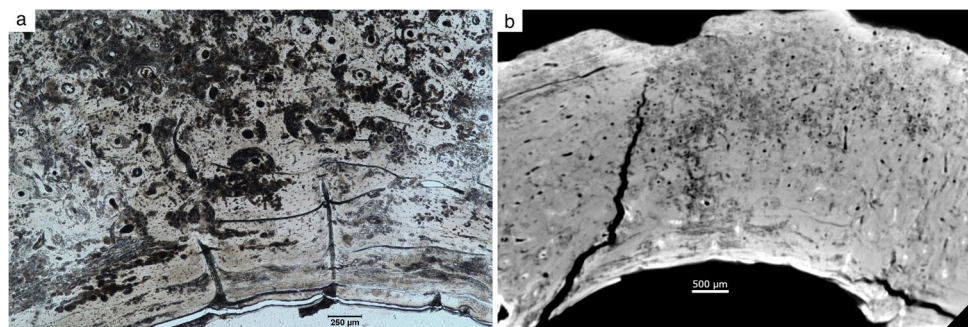
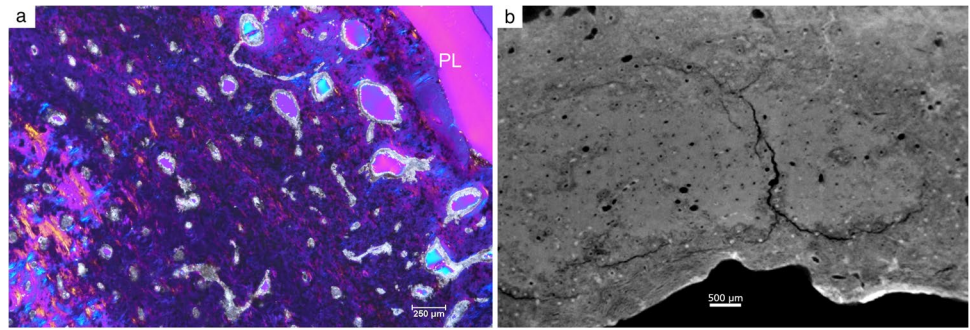


Fig. 6 Sample R03, an adult of unknown sex. **a** Light micrograph of midline and periosteum of a transverse histological thin section (lambda plate under 4(1×) magnification). **b** Single virtual transverse cross-Sect. (1 voxel [8.0 μm] thick) through a microCT image showing midline, and endosteal surface

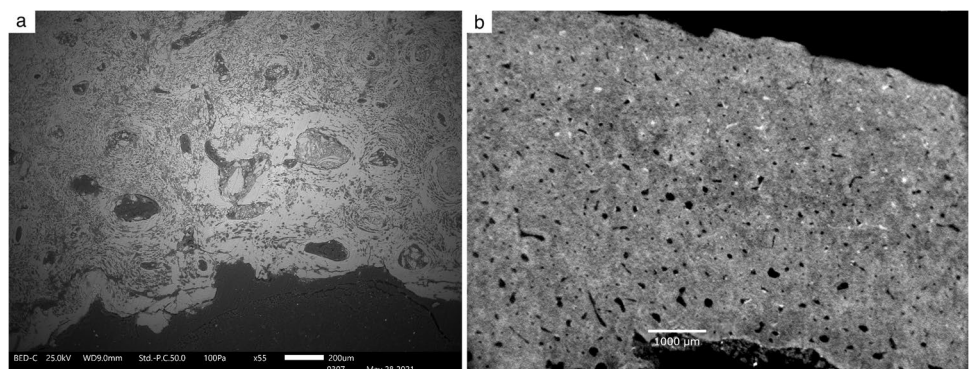


Virtual cross-sections The bone has undergone bioerosion in large patches. Canals remain, particularly along the midline, but bioerosion is pervasive throughout and between virtual slices through the 3D image, particularly along the endosteum and towards the periosteum. Though bioerosion attacks the concentric lamellae, rings of denser bone separate erosion from the canals. Along the midline where bone remains better preserved, lamellae of Haversian systems are visible as are faint cement lines. Many canals are filled with dense (white) inclusions (calcite) in areas of heavy and light bioerosion. Circumferential lamellae, particularly along the endosteum, are heavily affected. The outer layer of the endosteum is also denser. Two large shrinkage-induced microfissures encircle the midline where bioerosion is arrested, as noted in the histology. The periosteal lamellae are eroded but are slightly denser than the endosteal lamellae.

GÖ03/femur (OHI 0/VHI 0) (Fig. 7)

OHI with SEM The bacterial attack is extensive. MFDs are identifiable along the entire section with only Haversian canals remaining. A very small area of well-preserved bone remains along the endosteum; however, this surface is heavily eroded. Most of the canals are filled with an exogenous matrix, possibly bone fragments, soil, and/or calcite. The periosteum is also heavily eroded.

Fig. 7 Sample GÖ03, a late mature-senile male. **a** BED-SEM image showing midline and endosteum. **b** Single virtual transverse cross-Sect. (1 voxel [8.0 μm] thick) through a microCT image showing midline, and endosteal and periosteal surfaces

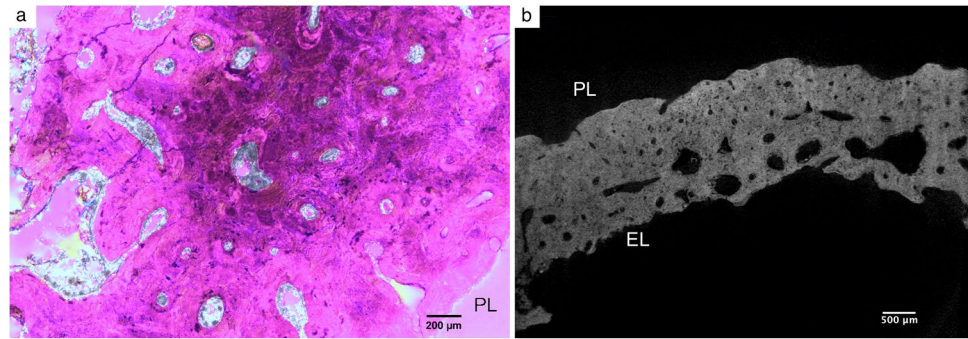


Virtual cross-sections The bone has undergone extensive bioerosion with little unaltered bone remaining. Small Howship's lacunae suggest incipient osteoporosis (Supplementary Material S6). Canals remain but bioerosion is extensive throughout and between virtual slices, and several are filled with a dense (white) material, particularly along the periosteum towards the midline. The periosteal circumferential lamellae have been sloughed; some remain along the endosteal surface, which is also encrusted with inclusions as are canals along this border. Although bioerosion affects the entirety of the sample, it is more prevalent (darker grey values) towards the periosteum where concentric lamellae can barely be distinguished, if at all, from the surrounding interstitial lamellae, and in a patch along the endosteum. Trails of lighter grey values where some visually undifferentiated lamellae of the Haversian systems can be seen are interspersed amongst heavy demineralization. In general, bioerosion is now so heavy that individual MFDs are indistinguishable.

S04/femur (OHI 0/VHI 0.25) (Fig. 8)

OHI with LM Macroscopic examination revealed the individual to be osteoporotic; this was confirmed by histology. Bacterial attack is heavy; only Haversian canals are identifiable. There is no collagen preservation. There is exogenous mineral precipitation in most Haversian canals. Bioerosion is severe throughout the entire section. Exogenous sediment

Fig. 8 Sample S04, a late mature female. **a** Micrograph of midline and endosteum of a transverse histological thin section (lambda plate and 4(1.25 \times) magnification). **b** Single virtual transverse microCT cross-Sect. (1 voxel [4.0 μ m] thick) showing midline, and periosteal and endosteal surfaces



is attached to both the endosteal and periosteal surfaces with exogenous infilling along the endosteum.

Virtual cross-sections The sample has undergone extensive bioerosion with little unaltered bone remaining. Canals remain distinct but bioerosion is extensive throughout and between virtual slices; however, the bone is also porous and demineralized in part due to an osteoporosis-induced reduction in bone mineral density (Marcus and Bouxsein, 2010). Many canals exhibit clear evidence of resorption, such as Howship's lacunae and irregular borders. During senescence remodelling of Haversian systems, including smaller ones, results in the enlargement of canals and their coalescence (Seeman 2013) as found in this sample, and should not be confused with bioerosion. Patches of bioerosion (dark grey values) are present as are MFDs, which, upon closer inspection, appear to surround canals; however, because the concentric lamellae are indistinguishable, partly due to age, it is difficult to ascertain that MFD concentrates around canals. The circumferential lamellae of the periosteum and endosteum have been sloughed.

IN01/cremated femur (OHI 4.75/VHI 4.5) (Fig. 9)

OHI with LM Macroscopic examination revealed the sample was cremated as confirmed by histology. It appears that there is no bioerosion, though discoloration makes the assessment difficult. Osteocyte lacunae are numerous and slightly enlarged, which is a common feature of cremated bone.

Howship's lacunae are also visible (Supplementary Material S7). There is exogenous mineral precipitation within the Haversian canals. The collagen signal is weak (Supplementary Material S7). Overall, the classic characteristics of concentric lamellae are lost as the matrix becomes homogeneous due to cremation (Hunger and Leopold 1978; Schultz 1986).

Virtual cross-sections The consistently medium-dark grey grey-values of each virtual slice within the virtual stack (save for high density (bright white) exogenous mineral precipitation) confirm cremation; however, the evaluation was hindered by the inability to visualize certain anatomical features due to burning. The periosteal lamellae are missing, though some remain along the endosteum. Canals can be distinguished throughout, though they appear smaller than usual by visual inspection. However, a morphometric assessment is required to verify this. It is demonstrated that burning at medium-to-high/high temperatures results in shrinkage, cracking, and crystallisation (Hanson and Cain 2007; Boschin et al. 2015; Ellingham and Sandholzer 2020). Several long, narrow microfissures travel from both the periosteum and endosteum towards the midline; all are dense (whitish), which may be calcite. The visually undifferentiated lamellae surrounding Haversian canals are obscured by burning but are more clearly visible towards the endosteum and along the midline than the periosteum. That they remain visible may be due to the slightly denser cement lines that are visible around some Haversian systems.

Fig. 9 Sample IN01, an adult-mature female. **a** Light micrograph of midline and endosteum of a transverse histological thin section (plane-polarised light and 10(1 \times) magnification). **b** Single virtual transverse microCT cross-Sect. (1 voxel [10.9 μ m] thick) showing midline, and periosteal and endosteal surfaces

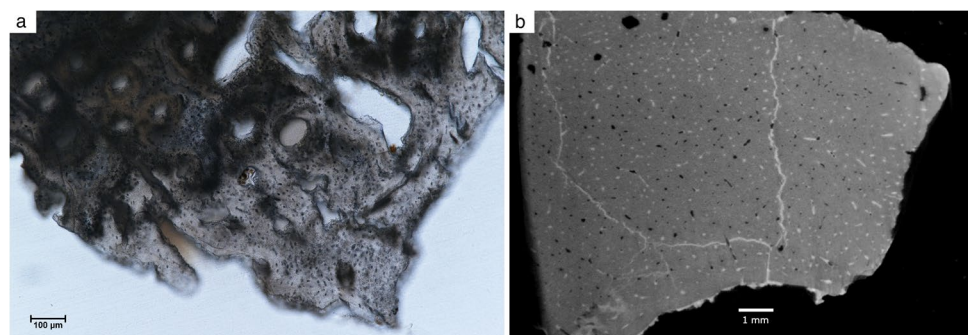
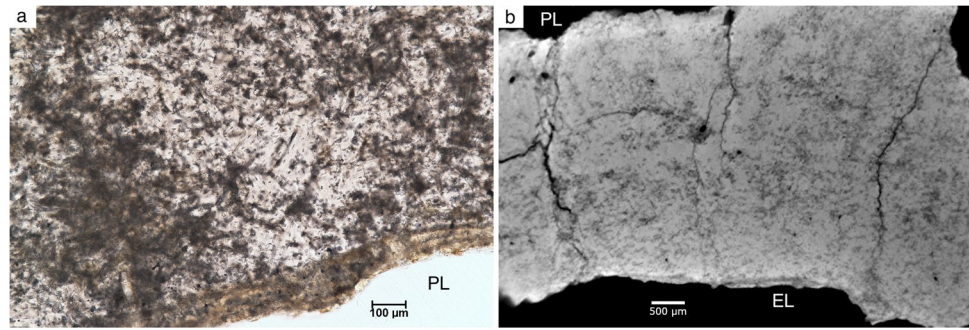


Fig. 10 Sample R04, a mammalian long bone. **a** Light micrograph of midline and endosteum of a transverse histological thin section (plane-polarised light and 10(1×) magnification). **b** Single virtual transverse microCT cross-Sect. (1 voxel [8 μm] thick) showing midline, and periosteal and endosteal surfaces



R04/faunal long bone fragment (OHI 3.5/VHI 3) (Fig. 10)

OHI with LM This bone was macroscopically identified as non-human. There is a clear pattern of bioerosion with MFD visible in patches throughout the entire section; however, bioerosion is inhibited. Under polarised light, a thick, high-density band can be seen along the periosteum and a thinner band along the endosteum. There is brownish staining along both surfaces. Haversian canals are visible in the histology, and the canaliculi are slightly enlarged (seen at higher magnifications, Supplementary Material S8). In areas without MFD, the lacunae are typical in size. Collagen preservation is poor even in the islands of bone that are free of MFD.

Virtual cross-sections The bone has undergone moderate bioerosion. Some circumferential lamellae, individually visually undifferentiated, remain along the endosteum and periosteum; both surfaces have light grey, higher density bands as noted in the histology. Bioerosion manifests in patches relatively evenly throughout and between virtual slices, with a slightly higher concentration along the midline. Although MFDs have spread throughout the sample, they remain distinct and do not generally present as undifferentiated dark grey patches. There are several shrinkage artefacts that primarily travel longitudinally from the periosteum. There are few canals, as expected for plexiform animal bone, and the few Haversian lamellae that are visible are difficult to distinguish. There is potentially also osteon banding between two longitudinal microfissures below the transverse crack along the midline.

Statistical results

The following results (Table 3) show that exact inter-observer matching within each histological index is at least 54% but diminishes across all observations. However, it is useful to also assess approximate and general observational matches, as the histological indices are categorical across several criteria. This approach elucidates the rate of approximate agreement of minimal variation and minor variation.

Table 3 Joint-probability of agreement calculations between OHI observations, VHI observations, and across all observations. Each set of calculations was analysed for an exact match, approximate match (within ≤ 0.5), and general match (within ≤ 1.0)

	Joint-probability of agreement ($n=28$)		
	Exact match	Approx. match (≤ 0.5)	General match (≤ 1)
OHI	54%	61%	96%
VHI	61%	82%	96%
Overall	21%	39%	93%

Table 4 Pearson correlation coefficient calculations between OHI observations, VHI observations, and the mean values of both OHI and VHI observations as the overall analysis

Index	Pearson correlation coefficient
OHI	0.94
VHI	0.96
Overall	0.97

Assessing for these minimal disagreements (≤ 0.5) demonstrates a significant increase in observation agreement for both OHI and VHI ratings. Furthermore, a general matching with a threshold of ≤ 1.0 between observations demonstrates a significant increase of all categories, with a minimum of 93% agreement.

The results of our PCC analyses (Table 4) demonstrate a strong positive (0.94) correlation between the OHI as rated by two observers, and a stronger positive (0.96) correlation between the VHI as rated by two observers, with a strong correlation overall (0.97) between the mean values of OHI and VHI observations. To account for observational agreement by chance, LOA analysis was performed. As histological indices are based on multiple criteria with multiple descriptive indicators, the problem of equifinality arises. This approach helps address the chance to which observers agree and assesses agreement based on genuinely similar observations using the same rating scale. The LOA analysis (Table 5) demonstrates that for the OHI, observer 1

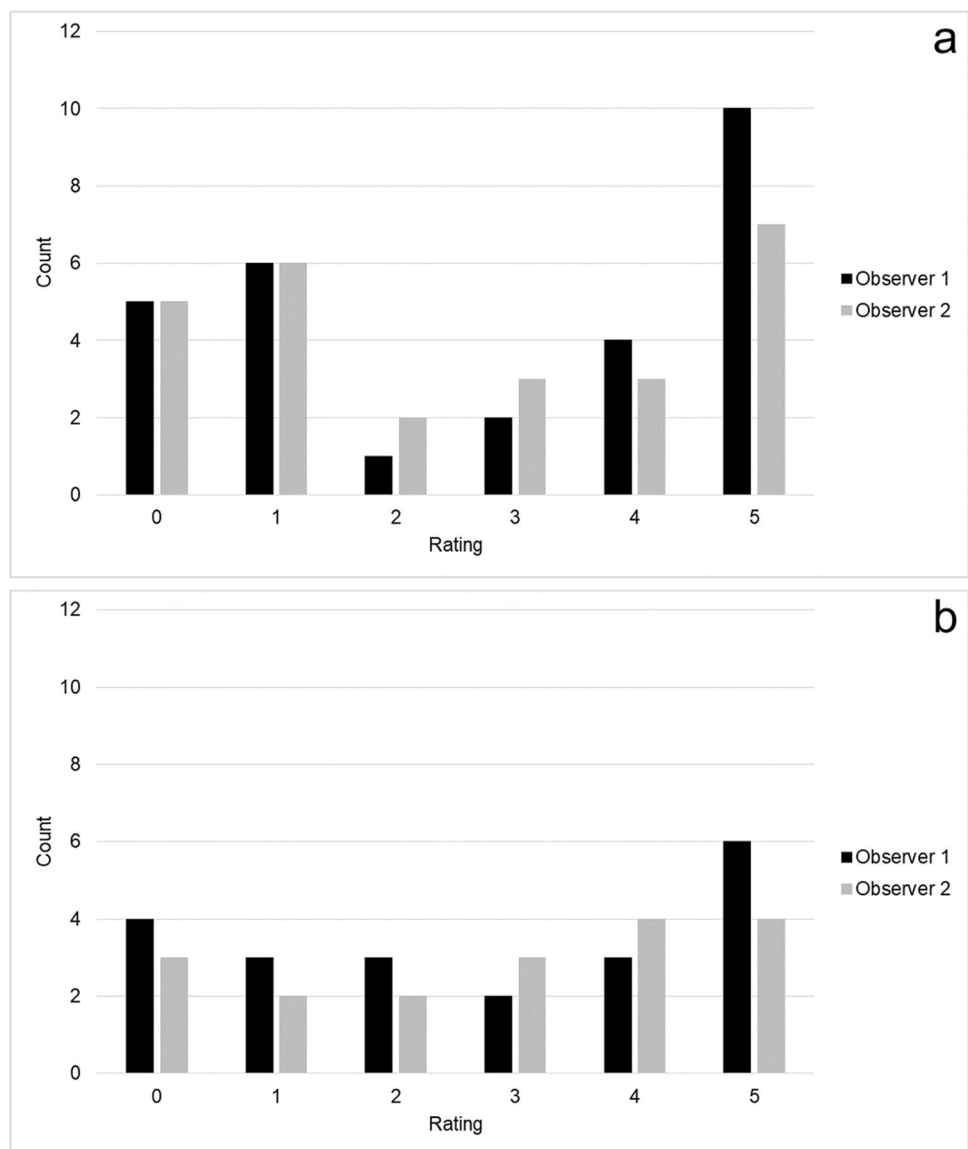
Table 5 Limits of agreement calculations of OHI, VHI, and the mean values of both OHI and VHI observations as the overall analysis

Limits of agreement			
	Average difference	Lower	Upper
OHI	0.25	-1.1244	1.62437
VHI	-0.02	-1.0888	1.05304
Overall	-0.04	-0.9681	0.87885

measures slightly biased (0.25), whereas for VHI observer 2 measures negligibly biased (-0.02). These negligible differences indicate that both observers produce relatively similar results, with a trend of observer 1 rating marginally higher observations (4 s and 5 s) and observer 2 rating slightly lower observations (1 s and 2 s) (Fig. 11a, b).

A 95% confidence interval is used to determine the limits of agreement across observations (see Bland and Altman 1986). For the OHI, the systematic difference is greater than the VHI observations (Fig. 11a, b) as indicated by the upper and lower limit ranges. One observation (GÖ25) falls outside the LOA for the OHI assessment (Fig. 12a); however, this is the only difference where the observers rated a specimen significantly different. Similarly, VHI observations were consistently matching, and observer bias is distributed evenly with 1 observation falling outside the limits of agreement: GE08 where observer 1 rated the sample higher than observer 2 (Fig. 12b). Furthermore, the trend across observations is similar for both the OHI and VHI where observer 1 tends to rate more specimens higher and observer 2 tends to rate more specimens lower (Fig. 12c). However, the OHI illustrates a

Fig. 11 Frequency of **a** OHI ratings per observer and **b** VHI ratings per observer



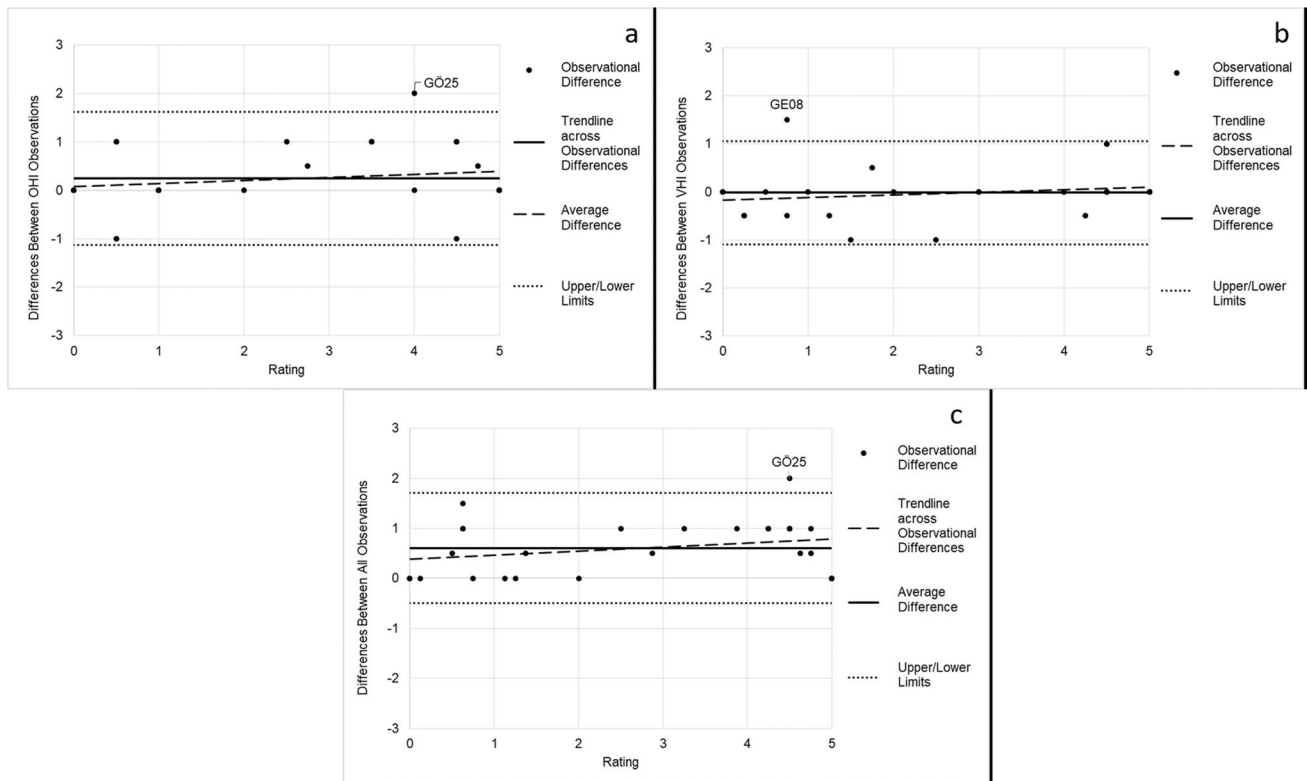


Fig. 12 Bland–Altman plot. **a** Differences between OHI observations. **b** Differences between VHI observations. **c** Differences between all observations

slightly more accentuated slope ($y = 0.0639x + 0.0753$) compared to the VHI ($y = 0.0537x - 0.1671$), demonstrating the minor differences in observations between the extreme ratings. This further shows that the observers are more prone to rate at either end of the scale and with minimal inherent bias in one observer compared to the other.

Discussion

The IRR results demonstrate that the VHI evaluation of virtual sections is congruent with the OHI rating of histological thin sections. As noted, certain structures taken into consideration by the OHI, such as individual concentric lamellae, cannot be differentiated, nor can structures smaller than $1 \mu\text{m}$ (e.g. osteocyte lacunae) be visualized without synchrotron-based microCT (Andronowski et al. 2017a,b), but undifferentiated concentric lamellae, and features such as shallow pits and tunnels can be seen with lab-based microCT. Moreover, our inability to visualize osteocyte lacunae may result from a contrast-to-resolution issue during the scan. Thus, the VHI is able to describe the level of bioerosion that a sample has undergone, specifically that which

results from bacterial attack. It may be possible that non-MFD bioerosion can be detected and differentiated with microCT images; however, the samples included in this study almost exclusively exhibited MFD, and not type 1 Wedl cyanobacterial-induced tunnelling, which is primarily found in aquatic environments, nor type 2. Importantly, in other respects the virtual images are also consistent with what has been qualitatively described in conventional thin sections.

Qualitative comparisons with histology

Jans et al. (2002) specify five categories of diagenetic alterations as visualized via histology: (1) presence and type of MFD; (2) presence of inclusions (e.g. sand, fungi, fram-boids); (3) presence of infiltrations, such as stains exogenous to the bone matrix; (4) presence of microfissures; and (5) birefringence intensity (see Fig. 1b). We found that MFD can be clearly visualized in virtual sections; these can, moreover, be virtually measured (as can anatomical features) to refine their identification by size (Fig. 13). Such measurements are possible due to the pixel-size calibration inherent in microCT scans (Withers et al. 2021). In badly affected samples, it is difficult to ascertain which type of tunnelling is present, as the bioerosion presents as large dark grey

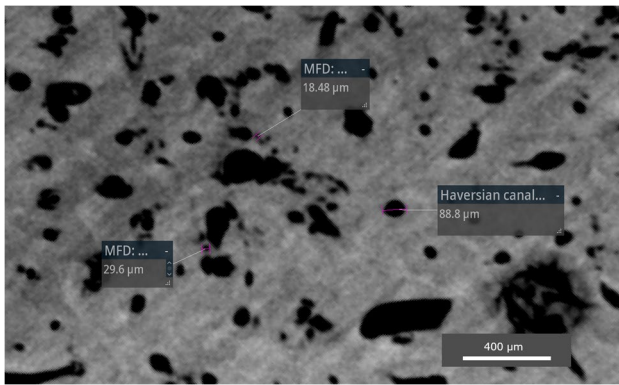


Fig. 13 Virtual measurements of MFD and Haversian canal in mid-line of a single virtual transverse cross-section. (1 voxel [8.0 µm] thick) of femoral sample GÖ01

patches. However, this problem is also encountered with thin section micrographs of badly preserved samples, and, moreover, though morphologically distinct, different MFDs are very likely, “all aspects of the same type of bacterial attack, differing only in tissue microarchitecture and local hydrology” (Turner-Walker 2019, p. 35). We were also unable to visualize the enlarged or stained canaliculi diagnosed via histology. This is likely due to the small size of the tunnels, which, although they may be long, are not thick enough to be visualized at the resolution we used.

We agree with Booth et al. (2016) that although inclusions can be observed based on differences in density (grey levels) and texture, no further identification of their composition can be made with benchtop microCT. Infiltrations such as stains are more difficult to distinguish in microCT images. While it may be possible to detect a stain after having been recognized through histology, it is not immediately apparent using virtual sections alone that a change in grey values results from, for example, the impregnation of inorganic substances as manifested macro- or microscopically as a stain, or if changes to the grey values result from demineralization caused by bacterial attack. Furthermore, while dissolution and recrystallization of HAp can be visualized as changes in grey values, it is not possible to determine the uptake or exchange of specific materials like uranium or fluorine, or nitrogen content, nor can microCT visualize the hypermineralized cuffs surrounding tunnels that result from mineral reprecipitation as is specifically achievable with SEM (Turner-Walker and Syversen 2002; Kendall et al. 2018). Microfissures recognized in histological sections can be clearly detected in virtual sections; it is also possible to determine if the microfissures are post-depositional, embedding artefacts, or result from excavation damage. Optical birefringence intensity cannot be assessed, though collagen content can be visualized with staining procedures not employed in this study (Hands Schuh et al.

2017). Lastly, virtual evaluation of sub-micron spongiform porosity (0.1–1 µm in diameter), a common form of tunnelling in archaeological bone (Turner-Walker et al. 2002; Turner-Walker 2012), requires SR-microCT (see Caruso et al. 2020, 2021) or synchrotron-based microscopy (Biswas et al., 2022).

As concerns qualitative descriptions of how bacteria invade bone, we once again find congruence between conventional microscopy and virtual imaging. Yoshino et al. (1991) describe regions heavily affected by bacteria and fungi as potentially corresponding to low X-ray density. As noted, areas of low density (dark grey values) that result from mineral dissolution and redistribution (Hackett 1981) correspond to MFD in the virtual sections. Yoshino et al. (1991) also report 5 to 10 µm in diameter vacuoles surrounding circumferential and Haversian lamellae, while Jackes et al. (2001) describe the orientation of MFDs along circumferential lamellae and the axis of Haversian systems. These vacuoles, or MFDs, were also visible in virtual sections within and surrounding the lamellae of Haversian systems and in circumferential lamellae. It has also been suggested that bacterial attack and chemical demineralization are impeded by cement lines (Turner-Walker et al. 2002; Turner-Walker 2012; Kendall et al. 2018). We may be visualizing this in samples such as GE08 (Supplementary Materials S9) where bioerosion appears to specifically attack the undifferentiated concentric lamellae, while in some regions of S01 (see Fig. 5) bioerosion seems to affect the interstitial lamellae, surrounding but not penetrating the concentric lamellae. However, there were no observable cement lines in sample S01. Moreover, after a certain point, when bioerosion has become severe, even if only within patches as with SB02 (Supplementary Materials S10), it is not possible to distinguish where bacterial attack begins or ends. Further research is thus required to confirm that bacterial attack is curbed by cement lines.

Effects of sampling

According to both Dal Sasso et al. (2014) and Booth et al. (2016), individual slices within a stack are representative of the sample, or entire femoral midshaft, and thus, the OHI applied to a single transverse cross-section may be “considered representative of the sample itself” (Dal Sasso et al. 2014, p. 37). We assessed the complete stack of virtual sections from microCT images and confirmed that within a given stack individual slices are generally homogeneously affected by bioerosion. While it appears probable that this holds true for the entire midshaft, further research should assess different regions of the femoral diaphysis to confirm homogeneity within the entire shaft, particularly when staining is present in patches.

Using microCT, Dal Sasso et al. (2014) found that skull, rib, and femur fragments present with different levels of bioerosion with femoral samples being the best preserved, and further suggest that the poorer preservation of rib and skull bone microstructure results from the higher volume of trabecular bone and porosity associated with the latter, which can be more heavily affected by inclusions and MFD. In the current study, we had both femoral and rib samples from only two individuals (GÖ01/GÖ24 (S11/S12) and GÖ04/GÖ25 (S13/S14)), none of which was badly affected by bioerosion; thus, we can neither confirm nor refute their findings. Nevertheless, our research suggests that, although the femoral diaphysis, which has a thick cortical layer, is preferred for visualizing canal structure and Haversian systems, the VHI can also be applied to mandibular, cranial, humerus, and rib samples.

As concerns burnt remains, Lemmers et al. (2020) conducted experiments to ascertain the visibility of bioerosion in histological sections of bone that had been cremated, concluding that it can be identified in burnt remains, though further research should investigate this to confirm these findings. Thus, the classical histological analysis provides good results; however, further experiments are required assessing the effects of burning on bioeroded versus uneroded remains in microCT images to better understand how bioerosion may be visualized in cremated remains. However, given the high concordance between the VHIs and OHIs of cremated samples, as demonstrated by the IRR, we included them in the dataset.

Conclusion

A strong correlation between histotaphonomy and virtual methods provides the first steps towards substantiating microCT for assessing microtaphonomy in archaeological bone. Though the evaluation of thin sections via light microscopy or SEM remains the best means to identify the presence and type of chemical and microbial diagenesis (e.g. collagen leaching using lambda filters, Wedl MFDs, and hypermineralized cuffs) affecting a sample, visualization with these methods entails time-consuming, labour-intensive, multi-step processes during any step of which artefacts may be accrued. Numerous 30 to 55- μm -thick slices must be sectioned with a microtome from an embedded sample with small areas of each section assessed individually. Moreover, transverse histological thin sections permit visualization in only a single direction. Although SR-microCT (Caruso et al. 2020, 2021), which can provide superior resolution, has also been used, it is not as readily accessible as lab-based microCT scanners, the costs of which are within the reach of start-up grants.

This study has demonstrated that microCT can be used as a complementary method to histology for the rapid,

accessible evaluation of bioerosion in archaeological bone, and for the screening of samples for further, more destructive analyses. The VHI method, like the OHI, remains subjective; however, the strong IRR results suggest that this is not a major problem. Further research may amalgamate the quantitative methods of Turner-Walker and Syversen (2002) with virtual techniques to improve accuracy and reproducibility. We also recommend that future analyses explore the effects of (1) cremation on the visualization of bioerosion, which has rarely been examined histologically (but see Hanson and Cain, 2007; Lemmers et al., 2020; Végh et al., 2021) as the presence or absence of bacterial attack may affect indices of cremation temperature, (2) the visibility of Wedl type 2 and cyanobacterial tunnelling in virtual sections, and (3) the applicability of other histological indices to microCT scan images. Lastly, the use of non-destructive and minimally invasive techniques extends the range of potential specimens to include very rare or fragile samples, and should be considered, where possible, before more destructive methods are employed to mitigate the ethical ramifications of sampling.

Supplementary Information The online version contains supplementary material available at <https://doi.org/10.1007/s12520-022-01563-w>.

Acknowledgements K.M. would like to thank Cordula Portmann and especially Magdalena Müller-Gerbl, Peter Zimmermann, Mirelle Toranelli, and Andreas Ochsenbein from the Anatomy University Basel, Switzerland, for training and support during thin section preparation. Thanks are also extended to Maciej Karwowski, Jarosław M. Czubak, Michaela Fritzl, Franz Pieler, Veronika Holzer, Karin Wilttschke-Schrotta, and the Austrian Federal Monuments Office for providing the archaeological samples. We kindly thank Mihaela Pavličev for granting access to the microCT scanners at the Unit for Theoretical Biology in the Department for Evolutionary Biology at the University of Vienna. Scanning electron microscopy was performed at the Core Facility of Cell Imaging and Ultrastructure Research (CIUS), University of Vienna, member of the Vienna Life-Science Instruments; we therefore kindly thank Daniela Gruber and Siegfried Reipert. Thanks are extended to Irene Lichtscheidl and her team from the CIUS facility for her major support and for providing the light microscope. K.M. and K.S.D.C. would particularly like to thank Marishka, Lilly, and Grögar, without whom this paper would not be possible. We would like to thank Suzanne Freilich for comments and suggestions. Lastly, we would also like to thank the reviewers for their comments and careful, critical reading of the manuscript, which added significant clarity to the paper, improving our identification, and broadening our understanding, of micro-taphonomic effects.

Author contribution Kirsten Mandl: conceptualization, methodology, validation, investigation, data curation, writing—original draft, visualization, project administration, funding acquisition; Kellie Sara Duffett Carlson: conceptualization, methodology, software, validation, investigation, data curation, writing—original draft, visualization, project administration; David Brönnimann: investigation, resources; Ashley McCall: formal analysis, writing—review and editing; Martin Grassberger: validation; Maria Teschler-Nicola: resources, writing—review and editing; Estella Weiss-Krejci: resources, writing—review and editing, funding acquisition; Brian Metscher: methodology, software, validation, writing—review and editing, supervision, project administration.

Funding Open access funding provided by University of Vienna. This paper is part of a dissertation project and sponsored by the Vienna Doctoral School of Ecology and Evolution (VDSEE) 2021-Completion Grant of the University of Vienna awarded to K.M. Thin section preparation was funded by the DEEPDEAD project (Deploying the Dead: Artefacts and Human Bodies in Socio-Cultural Transformations) under the HERA Joint Research Programme “Uses of the Past” (UP) (Collaborative Research Project (CRP) no. 15.055) and the European Union’s Horizon 2020 research and innovation programme under grant agreement No. 649307.

Data availability All original data are available in the online supplementary information.

Code availability Not applicable.

Declarations

Ethics approval Not applicable.

Consent to participate Not applicable.

Consent for publication Not applicable.

Conflict of interest The authors declare no competing interests.

Open Access This article is licensed under a Creative Commons Attribution 4.0 International License, which permits use, sharing, adaptation, distribution and reproduction in any medium or format, as long as you give appropriate credit to the original author(s) and the source, provide a link to the Creative Commons licence, and indicate if changes were made. The images or other third party material in this article are included in the article’s Creative Commons licence, unless indicated otherwise in a credit line to the material. If material is not included in the article’s Creative Commons licence and your intended use is not permitted by statutory regulation or exceeds the permitted use, you will need to obtain permission directly from the copyright holder. To view a copy of this licence, visit <http://creativecommons.org/licenses/by/4.0/>.

References

- Aigouy B, Mirouse V (2013) ScientiFig: a tool to build publication-ready scientific figures. *Nat Methods* 10(11):1048. <https://doi.org/10.1038/nmeth.2692>
- Andronowski JM, Pratt IV, Cooper DML (2017a) Occurrence of osteon banding in adult human cortical bone. *Am J Phys Anthropol* 164(3):635–642. <https://doi.org/10.1002/ajpa.23297>
- Andronowski JM, Mundorf AZ, Pratt IV, Davoren JM, Cooper DML (2017b) Evaluating differential nuclear DNA yield rates and osteocyte numbers among human bone tissue types: a synchrotron radiation micro-CT approach. *Forensic Sci Int Genet* 28:211–218. <https://doi.org/10.1016/j.fsigen.2017.03.002>
- Baier W, Mangham C, Warnett JM, Payne M, Painter M, Williams MA (2019) Using histology to evaluate micro-CT findings of trauma in three post-mortem samples — first steps towards method validation. *Forensic Sci Int* 297:27–34. <https://doi.org/10.1016/j.forsciint.2019.01.027>
- Balzer A, Gleixner G, Grupe G, Schmidt H-L, Schramm S, Turban-Just S (1997) *In vitro* decomposition of bone collagen by soil bacteria: the implications for stable isotope analysis in archaeometry. *Archaeometry* 39(2):415–429. <https://doi.org/10.1111/j.1475-4754.1997.tb00817.x>
- Biswas PP, Turner-Walker G, Rathod J, Liang B, Wang C-C, Lee Y-C, Sheu H-S (2022) Sustainable phosphorus management in soil using bone apatite. *J Environ Manage* 305:114344. <https://doi.org/10.1016/j.jenvman.2021.114344>
- Bland JM, Altman DG (1986) Statistical methods for assessing agreement between two methods of clinical measurement. *Lancet* 327(8476):307–310. [https://doi.org/10.1016/S0140-6736\(86\)90837-8](https://doi.org/10.1016/S0140-6736(86)90837-8)
- Booth TJ (2016) An investigation into the relationship between bacterial bioerosion and funerary treatment in European archaeological human bone. *Archaeometry* 58(3):484–499. <https://doi.org/10.1111/arc.m.12190>
- Booth T (2017) The rot sets in: low-powered microscopic investigation of taphonomic changes to bone microstructure and its application to funerary contexts. In: Erickson D & Thompson T (eds) *Human remains: another dimension: the application of imaging to the study of human remains*. Academic Press, London, pp. 7–28. <https://doi.org/10.1016/b978-0-12-804602-9.00003-5>
- Booth TJ, Redfern RC, Gowland RL (2016) Immaculate conceptions: micro-CT analysis of diagenesis in Romano-British infant skeletons. *J Archaeol Sci* 74:124–134. <https://doi.org/10.1016/j.jas.2016.08.007>
- Boschin F, Zanolli C, Bernardini F, Princivalle F, Tuniz C (2015) A look from the inside: microCT analysis of burned bones. *Ethnobiol Lett* 6(2):258–266. <https://doi.org/10.14237/ebi.6.2.2015.365>
- Brönnimann D, Portmann C, Pichler SL, Booth TJ, Röder B, Vach W, Schibler J, Rentzel P (2018) Contextualising the dead – combining geoarchaeology and osteo-anthropology in a new multi-focus approach in bone histotaphonomy. *J Archaeol Sci* 98:45–58. <https://doi.org/10.1016/j.jas.2018.08.005>
- Caruso V, Marinoni N, Diella V, Berna F, Cantaluppi M, Mancini L, Trombino L, Cattaneo C, Pastoro L, Pavese A (2020) Bone diagenesis in archaeological and contemporary human remains: an investigation of bone 3D microstructure and mineral-chemical assessment. *Archaeol Anthropol Sci* 12:162. <https://doi.org/10.1007/s12520-020-01090-6>
- Caruso V, Marinoni N, Diella V, Possenti E, Mancini L, Cantaluppi M, Berna F, Cattaneo C, Pavese A (2021) Diagenesis of juvenile skeletal remains: a multimodal and multiscale approach to examine the post-mortem decay of children’s bones. *J Archaeol Sci* 135:105477. <https://doi.org/10.1016/j.jas.2021.105477>
- Child AM (1995) Towards an understanding of the microbial decomposition of archaeological bone in the burial environment. *J Archaeol Sci* 22(2):165–174. <https://doi.org/10.1006/jasc.1995.0018>
- Dal Sasso G, Maritan L, Usai D, Angelini I, Artioli G (2014) Bone diagenesis at the micro-scale: bone alteration patterns during multiple burial phases at Al Khiday (Khartoum, Sudan) between the Early Holocene and the II century AD. *Palaeogeogr Palaeoclimatol Palaeoecol* 416:30–42. <https://doi.org/10.1016/j.palaeo.2014.06.034>
- Damann FE, Jans MME (2017) Microbes, anthropology, and bones. In: Carter DO, Tomberlin JK, Benbow ME, Metcalf JL (eds) *Forensic microbiology*. Wiley, Chichester, pp 312–327
- Ellingham S, Sandholzer MA (2020) Determining volumetric shrinkage trends of burnt bone using micro-CT. *J Forensic Sci* 65(1):196–199. <https://doi.org/10.1111/1556-4029.14150>
- Fernández-Jalvo Y, Andrews P, Pesquero D, Smith C, Marín-Monfort D, Sánchez B, Geigl E-M, Alonso A (2010) Early bone diagenesis in temperate environments: Part I: surface features and histology. *Palaeogeogr Palaeoclimatol Palaeoecol* 288(1–4):62–81. <https://doi.org/10.1016/j.palaeo.2009.12.016>
- Hackett CJ (1981) Microscopical focal destruction (tunnels) in exhumed human bones. *Med Sci Law* 21(4):243–265. <https://doi.org/10.1177/002580248102100403>

- Handschuh S, Beisser CJ, Ruthensteiner B, Metscher BD (2017) Microscopic dual-energy CT (microDECT): a flexible tool for multi-channel ex vivo 3D imaging of biological specimens. *J Microsc* 267:3–26. <https://doi.org/10.1111/jmi.12543>
- Hanson M, Cain CR (2007) Examining histology to identify burned bone. *J Archaeol Sci* 34(11):1902–1913. <https://doi.org/10.1016/j.jas.2007.01.009>
- Hedges REM, Millard AR, Pike AWG (1995) Measurements and relationships of diagenetic alteration of bone from three archaeological sites. *J Archaeol Sci* 22(2):201–209. <https://doi.org/10.1006/jasc.1995.0022>
- Higgs ND, Glover AG, Dahlgren TG, Little CTS (2011) Bone-boring worms: characterizing the morphology, rate, and method of bioerosion by *Osedax mucofloris* (Annelida, Siboglinidae). *Biol Bull* 221(3):307–316. <https://doi.org/10.1086/BBLv221n3p307>
- Hollund HI, Jans MME, Collins MJ, Kars H, Joosten I, Kars SM (2012) What happened here? Bone histology as a tool in decoding the postmortem histories of archaeological bone from Castricum, The Netherlands. *Int J Osteoarchaeol* 22(5):537–548. <https://doi.org/10.1002/oa.1273>
- Hollund HI, Sjögren BM, KG, (2018) Dead and buried? Variation in post-mortem histories revealed through histotaphonomic characterisation of human bone from megalithic graves in Sweden. *PLoS ONE* 13(10):e0204662. <https://doi.org/10.1371/journal.pone.0204662>
- Hunger H, Leopold D (1978) Identifikation. Springer, Berlin
- Jackes M, Sherburne R, Lubell D, Barker C, Wayman M (2001) Destruction of microstructure in archaeological bone: a case study from Portugal. *Int J Osteoarchaeol* 11(6):415–432. <https://doi.org/10.1002/oa.583>
- Janaway RC (1996) The decay of buried human remains and their associated material. In: Hunter J, Roberts C, Martin A (eds) *Studies in crime: an introduction to forensic archaeology*. BT Batsford Ltd., New York, pp 58–85
- Jans MME (2008) Microbial bioerosion of bone – a review. In: Wisshak L, Tapanila L (eds) Springer, Berlin, pp 397–413
- Jans MME, Kars H, Nielsen-Marsh CM, Smith CI, Nord AG, Arthur P, Earl N (2002) In situ preservation of archaeological bone: a histological study within a multidisciplinary approach. *Archaeometry* 44(3):343–352. <https://doi.org/10.1111/1475-4754.t01-1-00067>
- Jans MME, Nielsen-Marsh CM, Smith CI, Collins MJ, Kars H (2004) The characterisation of microbial attack in archaeological bone. *J Archaeol Sci* 31(1):87–95. <https://doi.org/10.1016/j.jas.2003.07.007>
- Kendall C, HøierEriksen AM, Kontopoulos I, Collins MJ, Turner-Walker G (2018) Diagenesis of archaeological bone and tooth. *Palaeogeogr Palaeoclimatol Palaeoecol* 491:21–37. <https://doi.org/10.1016/j.palaeo.2017.11.041>
- Kontopoulos I, Nystrom P, White L (2016) Experimental taphonomy: post-mortem microstructural modifications in *Sus scrofa domestica* bone. *Forensic Sci Int* 266:320–328. <https://doi.org/10.1016/j.forsciint.2016.06.024>
- Le Garff E, Mesli V, Delannoy Y, Colard T, Demondion X, Becart A, Hedouin V (2017) Technical note: early post-mortem changes of human bone in taphonomy with μ CT. *Int J Legal Med* 131:761–770. <https://doi.org/10.1007/s00414-016-1509-y>
- Lemmers SAM, Gonçalves D, Cunha E, Vassalo AR, Appleby J (2020) Burned flesh or dry? The potential of bioerosion to determine the pre-burning condition of human remains. *J Archaeol Method Theory* 27:972–991. <https://doi.org/10.1007/s10816-020-09446-x>
- Marcus R, Bouxsein ML (2010) The nature of osteoporosis. In: Marcus R, Feldman D, Nelson DA, Rosen CJ (eds) *Fundamentals of osteoporosis*. Academic Press, Burlington, pp 25–34
- Metcalf JL, Zech XuZ, Weiss S, Lax S, Van Treuren W, Hyde ER, Jin Song S, Amir A, Larsen P, Sangwan N, Haarmann D, Humphrey GC, Ackermann G, Thompson LR, Lauber C, Bibat A, Nicholas C, Gebert MJ, Petrosini JF, Reed SC, Gilbert JA, Lynne AM, Bucheli SR, Carter DO, Knight R (2016) Microbial community assembly and metabolic function during mammalian corpse decomposition. *Science* 351(6269):158–162. <https://doi.org/10.1126/science.aad2646>
- Millard AM (2001) The deterioration of bone. In: Pollard AM, Brothwell DR (eds) *Handbook of archaeological science*. Wiley, Chichester, pp 633–643
- Müller R, Van Campenhout H, Van Damme B, Van Der Perre G, Dequeker J, Hildebrand T, Rügsegger P (1998) Morphometric analysis of human bone biopsies: a quantitative structural comparison of histological sections and micro-computed tomography. *Bone* 23(1):59–66. [https://doi.org/10.1016/s8756-3282\(98\)00068-4](https://doi.org/10.1016/s8756-3282(98)00068-4)
- Nielsen-Marsh CM, Smith CI, Jans MME, Nord A, Kars H, Collins MJ (2007) Bone diagenesis in the European Holocene II: taphonomic and environmental considerations. *J Archaeol Sci* 34(9):1523–1531. <https://doi.org/10.1016/j.jas.2006.11.012>
- Parker Pearson M, Chamberlain A, Craig O, Marshall P, Mulville J, Smith H, Chenery C, Collins M, Cook G, Craig G, Evans J, Hiller J, Montgomery J, Schwenninger J-L, Taylor G, Weiss T (2005) Evidence for mummification in Bronze Age Britain. *Antiquity* 79:529–546. <https://doi.org/10.1017/S0003598X00114486>
- Particelli F, Mecozzi L, Beraudi A, Montesi M, Baruffaldi F, Viceconti M (2012) A comparison between micro-CT and histology for the evaluation of cortical bone: effect of polymethylmethacrylate embedding on structural parameters. *J Microsc* 245(3):302–310. <https://doi.org/10.1111/j.1365-2818.2011.03573.x>
- Piepenbrink H (1986) Two examples of biogenous dead bone decomposition and their consequences for taphonomic interpretation. *J Archaeol Sci* 13(5):417–430. [https://doi.org/10.1016/0305-4403\(86\)90012-9](https://doi.org/10.1016/0305-4403(86)90012-9)
- Rühli FJ, Kuhn G, Evison R, Müller R, Schultz M (2007) Diagnostic value of micro-CT in comparison with histology in the qualitative assessment of historical human skull bone pathologies. *Am J Phys Anthropol* 133(4):1099–1111. <https://doi.org/10.1002/ajpa.20611>
- Schindelin J, Arganda-Carreras I, Frise E, Kaynig V, Longair M, Pietzsch T, Preibisch S, Rueden C, Saalfeld S, Schmid B, Tinevez J-Y, White DJ, Hartenstein V, Eliceiri K, Tomancak P, Cardona A (2012) Fiji: an open-source platform for biological-image analysis. *Nat Methods* 9:676–682. <https://doi.org/10.1038/nmeth.2019>
- Schultz M (1986) Die mikroskopische Untersuchung prähistorischer Skelettfunde: Anwendung und Aussagemöglichkeiten der differentialdiagnostischen Untersuchung (Archäologie und Museum Vol. 1,6). Retrieved October 8, 2021, from https://www.archaeologie.bl.ch/uploads/files/website/Die_mikroskopische_Untersuchung_praehistorische_Skelettfunde.pdf
- Schultz M (2001) Paleohistopathology of bone: a new approach to the study of ancient diseases. *Yearb Phys Anthropol* 44:106–147. <https://doi.org/10.1002/ajpa.10024>
- Seeman E (2013) Age- and menopause-related bone loss compromise cortical and trabecular microstructure. *J Gerontol A* 68(10):1218–1225. <https://doi.org/10.1093/gerona/glt071>
- Smith CI, Nielsen-Marsh CM, Jans MME, Arthur P, Nord AG, Collins MJ (2002) The strange case of Apigliano: early ‘fossilization’ of medieval bone in southern Italy. *Archaeometry* 44(3):405–415. <https://doi.org/10.1111/1475-4754.T01-1-00073>
- Turner-Walker G, Syversen U (2002) Quantifying histological changes in archaeological bones using BSE-SEM image analysis. *Archaeometry* 44(3):461–468. <https://doi.org/10.1111/1475-4754.t01-1-00078>
- Turner-Walker G, Nielsen-Marsh CM, Syversen U, Kars H, Collins MJ (2002) Sub-micron spongiform porosity is the major

- ultra-structural alteration occurring in archaeological bone. *Int J Osteoarchaeol* 12(6):407–414. <https://doi.org/10.1002/oa.642>
- Turner-Walker G (2012) Early bioerosion in skeletal tissues: persistence through deep time. *N Jb Geol Paläont* 265(2):165–183. <https://doi.org/10.1127/0077-7749/2012/0253>
- Turner-Walker G (2019) Light at the end of the tunnels? The origins of microbial bioerosion in mineralised collagen. *Palaeogeogr Palaeoclimatol Palaeoecol* 529:24–38. <https://doi.org/10.1016/j.palaeo.2019.05.020>
- Turner-Walker G, Peacock EE (2008) Preliminary results of bone diagenesis in Scandinavian bogs. *Palaeogeogr Palaeoclimatol Palaeoecol* 266(3–4):151–159. <https://doi.org/10.1016/j.palaeo.2008.03.027>
- Uchiyama T, Tanizawa T, Muramatsu H, Endo N, Takahashi HE, Hara T (1997) A morphometric comparison of trabecular structure of human ilium between microcomputed tomography and conventional histomorphometry. *Calcif Tissue Int* 61:493–498. <https://doi.org/10.1007/s002239900373>
- Végh EI, Czermak A, Márquez-Grant N, Schulting RJ (2021) Assessing the reliability of microbial bioerosion features in burnt bones: a novel approach using feature-labelling in histotaphonomical analysis. *J Archaeol Sci Rep* 37:102906. <https://doi.org/10.1016/j.jasrep.2021.102906>
- Wedl C (1865) Über einen im Zahnbein und Knochen keimenden Pilz. *Sitzungsberichte der mathematisch-naturwissenschaftlichen Classe der Kaiserlichen Akademie der Wissenschaften* 50(1864):171–193.
- White L, Booth TJ (2014) The origin of bacteria responsible for bioerosion to the internal bone microstructure: results from experimentally-deposited pig carcasses. *Forensic Sci Int* 239:92–102. <https://doi.org/10.1016/j.forsciint.2014.03.024>
- Withers PJ, Bouman C, Carmignato S, Cnudde V, Grimaldi D, Hagen CK, Maire E, Manley M, Du Plessis A, Stock SR (2021) X-ray computed tomography. *Nat Rev Methods Primers* 1:18. <https://doi.org/10.1038/s43586-021-00015-4>
- Yoshino M, Kimijima T, Miyasaka S, Sato H, Seta S (1991) Microscopical study on estimation of time since death in skeletal remains. *Forensic Sci Int* 49:143–158. [https://doi.org/10.1016/0379-0738\(91\)90074-s](https://doi.org/10.1016/0379-0738(91)90074-s)

Publisher's note Springer Nature remains neutral with regard to jurisdictional claims in published maps and institutional affiliations.